MONTE CARLO SIMULATION OF SURFACE RADIATIVE HEAT TRANSFER IN CAVITIES OF DOMESTIC GAS OVENS

Jair A. Torres, jair@labcet.ufsc.br
Renzo F. Figueroa, renzo@labcet.ufsc.br
Amir A. M. Oliveira, amir.oliveira@ufsc.br
Combustion and Thermal Systems Engineering Laboratory - LabCET
Mechanical Engineering Department - Federal University of Santa Catarina
Florianópolis, SC – Brazil

Abstract. *The analysis of newer designs of more efficient and effective ovens requires the modeling and optimization of the radiative heat transfer among surfaces whose radiation exchange is blocked by the presence of cooking trays. The Monte Carlo simulation of the thermal radiation exchange provides an effective cost-benefit ratio for performing the optimization of oven cavities with multiple surfaces with different positions and radiative properties. Here, the Monte Carlo simulation is applied to the calculation of view factors and net radiation heat transfer rates in oven cavities. Initially, a ray tracing algorithm to obtain the view factors is tested and validated for different configurations. A convergence analysis of the accuracy and dispersion of the results is done by comparison with available solutions resulting in error smaller than 0.4 % and standard deviations relative to the mean less than 0.0050 with 10.000 rays emitted. Then, the ray tracing algorithm is implemented for multiple view factors of the blocked rectangular cavity adding a multi-zones approach to tracing rays in geometry with obstacles. The boundary conditions for radiative simulations are provided by measurements of temperature in a conventional oven cavity, considering the required care in the measurement of the temperatures. The simulation shows high accuracy as well reaching values smaller than 0.3 % for 1 run of* 10^7 *rays. Following, a study of the field of radiation on the interior of cavity is developed. The gas burner oven is compared with an electric heating oven, showing a higher radiation exchange with the radiation source surface but lower uniformity over the load surfaces than that reached with electrical heating elements.*

Keywords: *Monte Carlo, Surface radiative heat exchange, Domestic gas ovens, Food cooking*

1. INTRODUCTION

The time and cost of the design of thermal devices can be substantially reduced by using numerical simulation of the relevant phenomena supported by measurements. In general, the analysis and optimization of new oven designs requires the capability of estimating heat transfer rates from oven to load in several configurations that include different dimensions, positions and radiative properties of the different surfaces that form the cavity and load. Within the cavity, the radiative heat transfer field is coupled to the convective heat transfer with the heated gases and conduction heat transfer along the plates that form the surfaces. The predictions are usually supported by measurements, but only for a few configurations and conditions. Although this problem may be modeled using a commercial CFD tool, the ability of performing many simulations in a flexible way and short time is important for product development. The Monte Carlo simulation of the thermal radiation exchange provides an effective cost-benefit ratio for performing the optimization of oven cavities with multiple surfaces with different positions and radiative properties, and is the first aspect of this.

This work presents a computational tool based on the Monte Carlo method to evaluate the heat transfer by radiation within a domestic gas oven, validated with literature data and supported by experimental measurements in a commercial model. A conventional domestic gas oven with inner cavity of 0.63 m x 0.47 m x 0.32 m (width x length x height) of black painted walls and transparent glass door was used for the experiments. An atmospheric burner of 3.05 kW using natural gas as fuel is centrally located below a removable bottom plate of the cavity. There are openings on the bottom plate to allow the flow of hot gas from the combustion chamber. The front door has an outer glass facing the ambient and an inner glass that faces the interior of the cavity. The operation of the oven in the experiments involved a regular knob and ignition system for ovens, which allows adjusting the oven power (or gas flow to the burner) at certain levels that result in certain estimated cooking temperatures. An inlet gas valve and a column manometer are used in order to control the line pressure to the burner. Representative works for the methodology applied in this study are provided by Viskanta & Toor (1968) , Maurente (2007), Luo, Hauer, & Day (2012) and Cheng, He, & Cui (2013).

In the following, the method, measurements and results are presented.

2. OVEN CAVITY AND MEASUREMENTS

2.1. Geometry and dimensions of the oven cavity

Figure 1.a. shows a diagram for the oven cavity and a cooking tray used in this study identifying the surfaces. The overall dimensions of the cavity are: W = 0.63 m, L = 0.47 m, and H = 0.32 m. The cooking tray is placed in the center of the cavity. The overall dimensions of the cooking tray (obstacle) are: w = 0.24 m, l = 0.345 m, and h = 0.04 m. The cavity bottom (at plane x-y, upon oven burner) is divided in surfaces 1, 2 and 3. The surface 1 is assumed with the same width of the obstacle. The cavity walls (at planes perpendicular to x-y plane) of the inferior half are numbered 4,

5, 6 and 7 where surface 7 corresponds to inferior half of oven door. The bottom of the tray viewing to inferior half of cavity, is surface 8. On the upper half, the numbering continues in a symmetric way, from 9 to 16. The top of the tray is surface 16 and the lateral tray walls are neglected for simplicity.

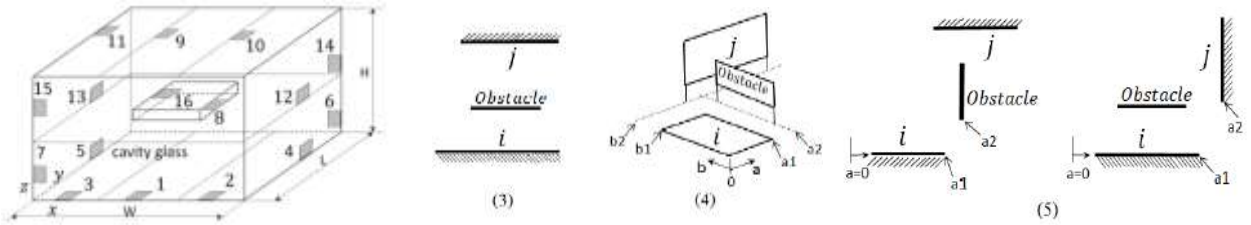

(a) (b)

Figure 1. Computational domain and test cases with obstacle

2.2 Measurements

As outlined before, the aim of this work is oriented to the study of the steady state in the cooking process of the oven cavity. Thus, surface and time averaged temperatures are used as follows. Initially, an average temperature of the last three minutes of the 45 min of the oven test measurements are obtained at different locations on each surface. The oven operation cycle used in all tests comprises of a preheating time of 15 minutes at maximum power (P1), followed by a cooking period of 30 min at intermediate power (P3). After 45 min, the oven is turned off and the test is considered complete. In total 32 thermocouples were fixed at the cavity walls, one close to each corner of the cavity (around 0.14 m) and one more in the center of each wall, additionally on the bottom plate in the region directly above the burner were fixed two more thermocouples. 29 thermocouples were fixed by the red silicon and the 3 thermocouples in the region above the burner were fixed additionally with 3/16" diameter stainless steel bolts and nuts. Type K thermocouples (chromel/alumel, Omega Engineering™) and an Agilent 34970A Data Acquisition System were used. All the thermocouples and the measurement system (Agilent) were simultaneously calibrated in a thermostatic bath in the temperature range from 20 °C to 400 °C with a maximum uncertainty in the measurement for all thermocouples within $\pm 2\ ^{\circ}C$. Once the measured steady-state surface temperatures are obtained at each location on each surface, each temperature is associated with a part of the total area and the surface temperature is obtained by surface averaging of the respective black-body emissive powers. A fourth square mean of the measured temperatures at each subsurface, $T_{m,s}$, is calculated according to Eq. (1) where T_i is the time averaged temperature and A_i the sector area of the i-th thermocouple on the sub-surface considered. A_s is the sub-surface area equal to ΣA_i .

$$T_{m,s} = \left[\frac{1}{A_s} \sum A_i T_i^4 \right]^{1/4} \tag{1}$$

Different values of sector areas Ai were tested in order to check the sensitivity of the averaged temperature to the sector area. Since there is a higher effect of the temperatures with the fourth power than of the sector area, the different choices of areas A_i resulted in similar values of mean temperatures. The 2 shows the results of these mean temperatures relative to the temperature of the burner-sub-surface (equal to 339°C) for each one of the sub-surfaces of the computational domain of simulations. The detector temperature is assumed 100 °C in order to study the behavior of the oven cavity with a tray at the cooking temperature and by simplicity the temperatures used for all locations of the radiation field were the mean temperatures computed for the center location.

		S6	0.49						
S5	0.47	S3	0.45	S1	1.00	S2	0.41	S4	0.48
		S7	0.32						

(a)

		S6	0.52						
S5	0.51	S3	0.53	S1	0.55	S2	0.53	S4	0.51
		S7	0.41						

(b)

Figure 2 Schematic of the non-dimensional mean temperatures Ti/T1 of each cavity sub-surface (S) used in simulations (a) inferior half of cavity (b) superior half of cavity. Non-dimensional detector temperature=0.30.

Lastly, the detector sub-surfaces are assumed with emittances close to a blackbody (0.95) while the emittances of the whole sub-surfaces of the cavity are assumed with 0.9 as an initial study case closer to the oven experimentally tested. From a preliminary experimental study, it is known that the global hemispherical emissivities of each surface of the cavity are around 0.9 (OLIVEIRA; PEREIRA, 2011).

3. METHOD

3.1 View factors of pair of surfaces

In the Monte Carlo approach, the surface forming the enclosure is divided into a number of j surfaces. The total radiative energy leaving a source surface *i* is discretized in N_i radiation packets of energy. Each radiation package leaves surface i and, eventually, after many reflections, is absorbed by a surface j. The view factor F_{i-j} expresses the fraction of energy leaving an area A_i that is absorbed by area A_j. In order to calculate the view factors, the surfaces may be assumed black and then the view factor may be understood as the probability of a random packet leaving surface i to reach surface j. Denoting N_{ij} as the number of packets leaving i that reach j and N_i as the total number of packets emitted, the view factor is estimated from

$$F_{i-j} = \lim_{N_i \to \infty} \left(\frac{N_{ij}}{N_i} \right) \approx \left(\frac{N_{ij}}{N_i} \right)_{N_i >> 1} \tag{2}$$

when N_i is a large number. Defining a ray as the straight path from surface i to surface j, the Monte Carlo Ray Tracing (MCRT) for view factors resolve the geometrical problem in determining the N_{ij} .

Because of the random nature of simulations the view factor reached with the same geometry and the same number of rays fluctuates with a level of dispersion dependent of the amount of rays used. The following results use a mean view factor $F_{i-jmean}$ of 100 runs of the algorithm for each number of rays N as is expressed in equation (3).

$$F_{i-jmean}\Big|_N = \frac{1}{n} \sum_{k=1}^{n} F_{i-jk}\Big|_N \qquad k = 1,2...100 \tag{3}$$

In equation (3), F_{i-jk} is the view factor reached in the k-th run of the simulation with N rays emitted. Notice that the total number of rays emitted for each mean view factor simulation is nxN rays.

View factors (VF) between two plane and rectangular surfaces at different configurations including the presence of obstacle can be calculated with the algorithm implemented at this work, which was based on an algorithm for two parallel aligned surfaces proposed by Nellis and Klein (2009). Once the number N_i of radiation packets of equal energy and the coordinates of surfaces are defined, the ray tracing algorithm for *uniform diffusive radiation* exchange can be divided in the following general steps: (1) Generate a random location of emission from a source surface i $(X_i, Y_i, 0)$, (2) Generate a random direction of emission (θ, Φ), (3) Find the intersection between ray r and the infinite plane containing a target surface j (X_J, Y_J, Z_J), (4) Check if intersection falls within the finite surface j. In case affirmative, the $Ni-th$ radiation packet is added to the radiation packets that already reached the surface j $(Nij = Nij + 1)$. Return to step (1) and send out another ray. After a sufficient number of rays have been emitted, the View Factors can be computed using Equation (2).

The view factors are evaluated and compared to algebraic solutions for a number of simpler configurations (test cases) covering all the possible arrangements between each pair of surfaces on the computational domain presented in Fig. 1 The ray tracing algorithm was implemented for two surfaces i and j allowing to calculate view factors with blocked elements (obstacles), non-aligned and non-common edge surfaces. The auxiliary coordinates (axis a and b) for perpendicular surfaces are indicated to illustrate the only constraints for the surface location which the algorithm requires, where the conditions a2 > a1 and b2 > b1 are always satisfied.

A study of the statistical error of the simulations as the number of rays Ni is increased was carried out for view factors in different configurations in order to test and validate the MCRT algorithm. Here the use of "statistical error" is more general that the same term used by Wang and Modest (2007). Wang and Modest apparently related this term only with the "precision" of simulations instead of the "general error- accuracy and precision" referred here.

The convergence is studied here considering, first, the comparison of the mean view factors reached with available solutions, and, second, the spread relative to the these mean values. A similar and brief approach studying the statistical error of the Monte Carlo method is presented by Modest (2003).

Reference values for the view factors *Fref* were obtained from algebraic solutions and from the area integration method (2AI) presented by Howell (2010) and Oliveira (2014), depending on the pair of surfaces analyzed. The percent deviation (p.d %) to *Fref* is defined as

$$p.d(\%) = \frac{F_{i-jmean} - Fref}{Fref} x100 \tag{4}$$

In order to evaluate the spread of the response around the mean (the precision), the standard deviation for a normal distribution is used similarly to the approach proposed by Wang and Modest (2007) for the heat flux in non-gray radiation in combustion gases. Thus, the standard deviation relative to the mean view factor of n runs with N rays can be expressed by Eq. (5) where F_{i-jk} and $F_{i-jmean}$ are defined by Eq. (3).

$$s\big|_N = \left(\frac{1}{n} \sum_{k=1}^{n} \left(F_{i-j,k}\big|_N - F_{i-j,mean}\big|_N \right)^2 \right)^{\frac{1}{2}} \quad k = 1,2...100 \tag{5}$$

3.2 View factors of cavity surfaces

In order to calculate all view factors for the computational domain illustrated in Figure 1, the MCRT algorithm was implemented for multiple rectangular surfaces at different configurations adding the multi-zones approach given by Coelho, Goncalves and Carvalho (1998) to tracing rays among multiple surfaces in a geometry with obstacles. The proposed approach, compared with the preceding simulations, simplified substantially the definition and input of the coordinates. Thus, the time required to compute view factors for certain number of surfaces in an enclosure is significantly reduced. In the multi-zones algorithm a ray Ri (or radiation packet) is traced until reaching multiple target surfaces from one source surface i in a volume zone (Fig. 3.a). A volume zone is represented here as a general domain formed by six orthogonal planes and each plane with one (or more) surfaces, such that any surface in that zone is not blocked by any obstacle. Fig 3.b shows a transversal section of two volume zones (Zone 1 and Zone 2) that are blocked by an obstacle. Now a ray emitted from the surface i can be intersected (or blocked) by a surface of zone 1 (ray R1), or it may pass to zone 2 without intersecting (rays R2 and R3). In zone 2 the ray again can be intersected (ray R2) or escape from the domain (ray R3). Hence the problem of tracing rays in multiple zones and obstacles can be solved by a number of simple problems involving multiple non-blocked surfaces.

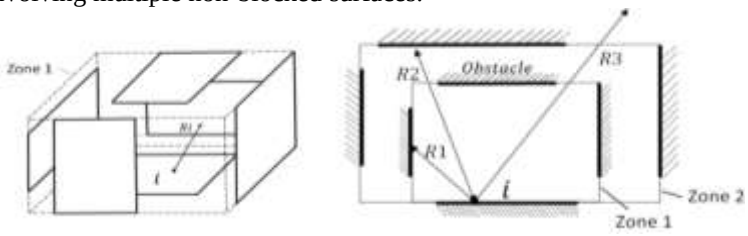

(a) (b)

Figure 3 Volume zones for MCRT algorithm of multiples surfaces (a) Three dimensional model for one volume zone (b) Two volume zones simulating view factors with obstacles

3.2 Heat Transfer Exchange

A distribution of the RHT (field of radiation) in the oven cavity is simulated adding the obstacle condition at different locations along the plane of cooking tray (half height of cavity) with a hypothetic short surface of a detector. For this purpose, the MCRT for VF algorithm for multiple surfaces and the thermal circuit analogy are used. A computational domain similar to that presented in Fig. 1.a is adopted, now increasing the dimensions for sub-surfaces 1 and 9 from 24 to 33 cm and defining the obstacle rectangular area (detector) by 12x12 mm^2. The dimensions of the cavity (63x47x32 cm) and the lateral sub-surfaces remain equal. Surfaces 8 and 16 can be seen as the hypothetical detector oriented in two directions: to the top and to the burner sides of cavity, respectively. Hence, the thermal network is built among 16 sub-surfaces as will be detailed below. Fig 4 shows the locations simulated for the detector indicating the sector of area of the cooking tray simulated in the previous sections (inner rectangle). The locations are symmetric in both axis x_c and y_c and some coordinates are listed.

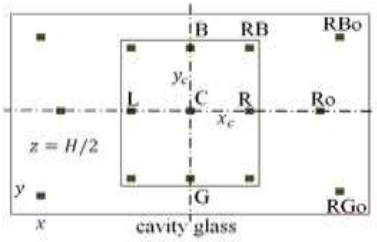

		x_c / W	y_c / L
C	center	0.00	0.00
R	right	0.16	0.00
B	back	0.00	0.32
RB	right back corner	0.16	0.32
Ro	right outside tray	0.36	0.00
RBo	right back outside	0.41	0.38
G	glass	0.00	-0.32

Figure 4. Locations of the detector at x-y plane with coordinates relative to the detector located in the geometric center for the radiation field simulation (not in scale)

The thermal circuit analogy based on the radiation network method is used to calculate radiative heat transfer (RHT) in rectangular enclosures with diffuse, opaque and gray surfaces. Regard an enclosure of S surfaces with a

temperature T, blackbody emissive power E_b, radiosity J and radiative heat transfer $Q_{ri\to j}$ between them. The net radiative heat transfer from a surface i, $Q_{n,i}$, and the radiative exchange with the remaining surfaces j, $Q_{r,i\to j}$, are defined and related by the conservation of energy according to Equation (6), where $F_{i\to j}$ are the diffuse view factors and the terms in square brackets are the resistances for the thermal circuit . Hence, view factors, temperatures and emittance of the sub-surfaces of the computational domain proposed were required in order to solve Equation (6) for 16 surfaces, using the software EES.

$$Q_{n,i}=\frac{E_{b,i}-J_i}{\left[\frac{1-\varepsilon_i}{A_i\varepsilon_i}\right]}=\sum_{j=1}^{S}Q_{r,i\to j}=\frac{J_i-J_j}{\left[\frac{1}{A_iF_{i\to j}}\right]} \tag{6}$$

The following results use a radiative exchange factor (REF) defined as the RHT absorbed (or emitted) by specified target surfaces $q_{i\to j}$ (or $q_{n,j}$) irrespective to the proportions of the RHT emitted by the burner sub-surface $q_{n,1}$ (see Eq.), similar to the approach given by Shaughnessy and Newborough (1998) with the RHT from heating elements in electrical ovens. A comparable expression to Eq. can be defined for the $REF_{n,j}$. The $q_{n,1}$ shown be unaffected by the detector relocation reaching values of $5170\pm 2\ W/m^2$ in all cases.

$$REF_{i\to j}=\frac{q_{i\to j}}{q_{n,1}}=\frac{A_iF_{i\to j}(J_i-J_j)}{A_j\left[\frac{\varepsilon_1(E_{b,1}-J_1)}{1-\varepsilon_1}\right]} \tag{72}$$

4. RESULTS ANS ANALYSIS

4.1 Accuracy and precision of MCRT for view factors of pairs of surfaces

Table 1 lists the view factors calculated for each test case considered in the convergence study. The reference value *Fref* was obtained from algebraic solutions for cases 1 and 2 and from the area integration method (2AI) for cases 3 to 5. Additionally, in the last two rows the mean view factors with 10^4 rays reached by the MCRT simulation as well as the percent deviation (p.d %) to *Fref* are presented. The aim of the results presented here are to test the algorithm implemented and not to perform a rigorous analysis of the influence of each configuration in the response of the simulations. The results presented in Table 1 are considered a satisfactory sample of the general statistical behavior found.

Table 1. View factors used in the convergence study

Case	1		2		3		4		5	
F(i,j)	F(1,8)	F(10,2)	F(11,5)	F(13,11)	F(1,9)	F(10,3)	F(13,7)	F(14,5)	F(4,13)	F(3,15)
Fref	0.3280	0.1717	0.0654	0.2772	0.0198	0.0027	0.0511	0.0381	0.0233	0.0495
MCRT[1]	0.3274	0.1717	0.0653	0.2777	0.0204	0.0028	0.0509	0.0384	0.0235	0.0499
p.d. %	0.2	0.0	0.1	0.2	3.2	3.9	0.4	0.8	0.9	0.8

[1] Mean value of n=100 runs with N=10^4 rays emitted

Figure 5.a shows the results for the mean view factors of test cases 1 and 2 (black and blue markers respectively) in comparison with the algebraic solutions (Howell, 2010). The simulation showed high accuracy reaching values less than $\pm 0.4\%$ for more of 10^4 rays emitted. Also, for more of 10^5 rays the tendency to approach the exact solution when the number rays goes to infinity is evidenced. Similar results were reached for other configurations tested when algebraic solutions were available. Figure 5.b shows the comparative results between the MCRT simulations and those by Oliveira (2014) with the 2AI method. One view factor for each test case is presented (black, blue and green markers for cases 3, 4 and 5 respectively). For test cases 4 and 5 between 10^3 and 10^4 rays the highest difference was of 3,5% for the F(13,7) indicated on the left of figure with a red circle. For more of $20x10^3$ rays (highlighted with red arrows) the percentage differences reached were of $\pm 0.8\%$. In both test cases again, the tendency to reach an exact solution when the number rays goes to infinity is evidenced for more than 10^5 rays emitted. On the other hand, for test case 3 in view factor F(1,9) (and F(10.3) not shown here) similar results were obtained but displaced in the error axis around $+3\%$. This difference motivated choosing surfaces 1 (as well as surface 10) to test the approach of calculating full view factors using multiple surfaces. As it will be presented later on, apparently the largest influence on this difference fall in the accuracy reached by the 2AI method. Another reason could be attributed to the magnitude of these view factors,

which are the lowest among all the view factors of the computational domain proposed (256 view factors in total). It results in more susceptible variations in percentage errors than with the largest view factors. Finally, leaving aside the displacement in test case 3, for more of $20x10^3$ rays the mean view factors oscillates in the interval around of $\pm 1.0\%$ (range between blue dashed lines). Notice that these range repeats in the remaining test cases.

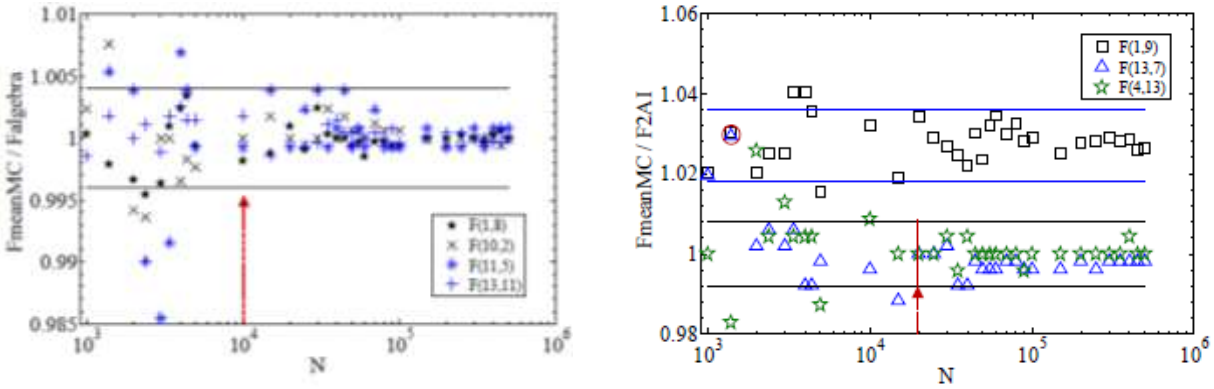

(a) (b)

Figure 5. Model validation against (a) algebraic solutions and (b) 2AI method

The convergence using Eq. (5) for view factors of the five test cases are summarized in Fig. 6. One view factor from each test case is plotted. As it can be seen, approximately the same gradient of spread over number of rays were observed in all cases. Similar results were reached for the remaining view factors listed in Table 1. View factors F(1,8) and F(1,9) (from test cases 1 and 3 respectively) shown approximately the highest and lowest standard deviations along all the number of rays simulated; similar behavior was observed with F(10,2) and F(10,3) (not plotted) from the same test cases. Apparently, the magnitude of the mean view factor is related with its spread in simulations, as it was shown in Table 1. The larger and smaller view factors were also from test cases 1 and 3 respectively. It can be observed from Fig. 6.a that the highest standard deviation in 10^4 and 10^5 rays were approximately of 0.0050 and 0.0015 respectively (See red remarks with F(1,8)), whereas for F(1,9) (and F(4.13) as well) were of 0.0015 and 0.0005 as indicated with the black arrows. There is an increment of precision of simulations as the number of rays is increased, which can be quantitatively measured with the variation of the standard deviation Δs for a certain view factor F_{i-j} .We can expect a similar decrease of the spread in simulations in all the mean view factors from the computational domain proposed. Fig. 6.b summarizes the results of the computational time spent in simulations. The view factors which in general demanded the lower and higher computational time among the view factors of Table 1 are shown (F(1,8) and F(14,5) respectively). The remaining view factors fall inside this range and they are not plotted for clarity. Specifically, the time measured for each number of rays corresponds to the simulation of one mean view factor of 100 runs of the MCRT algorithm. As it can be seen, the highest computational time never overtook 17 minutes (1000 s for $500x10^3$rays emitted). A 64-bit 3.10 GHz Intel Core i3 CPU was used for all simulations on this work. Finally, it is worth underline that the overall computational cost, in contrast to the requirements of accuracy and precision, depends on the significant number of view factors for the computational domain for the whole oven cavity (more of 200 for 16 surfaces). The pre- and post-processes of data in simulations is also time consuming. These last issues mainly motivated to implement the simultaneous and multiple surfaces approach described in the following section. Also, they provided the basis for choosing the number of rays in the subsequent simulations.

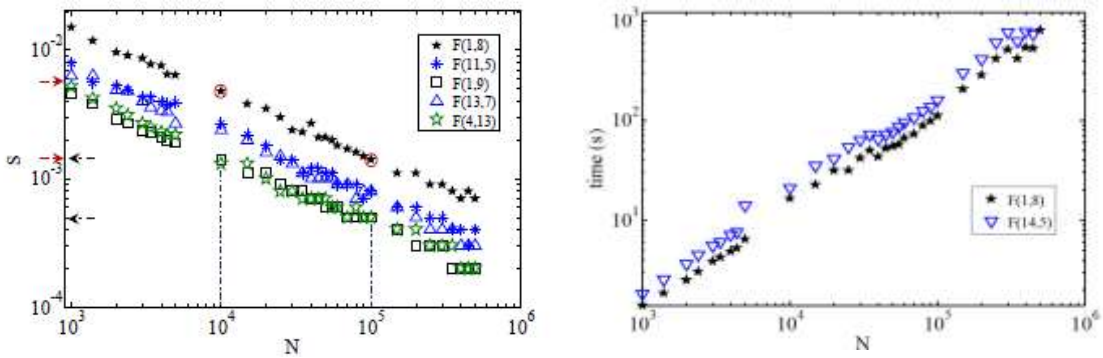

(a) (b)

Figure 6. Dispersion of MCRT and computational time as N is increased

4.2 View Factors for cavity surfaces

A multiple zones analysis was carried out for the computational domain of this work (16 sub-surfaces in total) taking the inferior and superior half of the cavity as two zones. One simulation allows to calculate 15 view factors from one determined rays emission surface. An appropriate origin and orientation of the coordinate system for the two volume zones defining an input matrix up to 35 coordinates for each volume zone were required at each simulation. Table 2 lists the view factors and the relative deviations with the algebraic solutions when available and with the 2AI method (marked with *) reached in the simulations for five surfaces (1, 5, 7, 10 and 16) of the oven cavity (fig 1.a) which with symmetry relations cover all the possible view factors for the entire computational domain. One run with 10^7 rays was considered appropriate for 16 view factors in the same simulation based on the study of convergence carried out before (notice that in 100 runs with 10^5 rays end up being equivalent in terms of total number of rays). The figures of the view factors were not rounded off in order to allow for crosscheck with the algebraic solutions when available and with the 2AI method. The zero values are known view factors non included in simulations. The sum rule for the view factors at each surface was also verified. The maximum computational time spend for one surface was of 22 hours. The simulation presented high accuracy, the relative deviations reached values that never exceed 0.3% when compared with the analytical solutions. In the case of non-algebraic solutions available comparing with the 2AI method, only three view factors exceeded 0.8% (in bold) .Two of them F(1,9) and F(10,3) are the same with the most differences found in the study of convergence presented in the section 4.1. The whole of the results with the MCRT simulation and the satisfaction of the sum rule suggest that that the view factors reached should be correct in contrast with the factors obtained from the 2AI method, whose sum reached 1.0000, 1.0218, 1.0041, 1.0147, 1.0001 for surfaces 1, 5, 7, 10 and 16 respectively.

Table 2 View factors for the oven cavity by the MCRT simulation and relative deviations to the Algebraic Solutions and 2AI Method*. The first column is the source surface i. The first row is the target surface j.

	View factors					Relative deviations (%)				
	S1	S5	S7	S10	S16	S1	S5	S7	S10	S16
S1	0	0.0567496	0.1482591	0.0621721	0	0	-0.2	0.0	0.4 *	0
S2	0	0.0122995	0.1036266	0.1715589	0	0	0.3	-0.1	-0.1	0
S3	0	0.2769932	0.1037836	0.0027946	0	0	-0.1	0.1	**3.5** *	0
S4	0.0380362	0.0509469	0.0956856	0.0652772	0	0.3	0.3	0.0	-0.1	0
S5	0.0378598	0	0.0957284	0.0139317	0	-0.2	0	0.0	0.2 *	0
S6	0.1323889	0.1282623	0.0975053	0.0493685	0	0.0	0.0	0.0	-0.3 *	0
S7	0.1325049	0.1282156	0	0.0494535	0	0.1	-0.1	0	-0.1 *	0
S8	0.3279005	0.0445102	0.0850431	0	0	0.0	0.1 *	-0.2 *	0	0
S9	0.0203621	0.0801784	0.0577868	0	0.4467108	**2.8** *	0.8 *	0.0 *	0	0.0
S10	0.0504934	0.0170176	0.0450984	0	0.1325127	0.4 *	0.2 *	0.2 *	0	0.0
S11	0.0504393	0.0796005	0.0448742	0	0.1325127	0.3 *	-0.4	-0.3 *	0	0.0
S12	0.0533687	0.0233338	0.0380171	0.2273435	0.0404865	-0.1 *	0.3 *	-0.2 *	0.0	0.2 *
S13	0.0533637	0	0.0379829	0.0100889	0.0403222	-0.1 *	0	-0.3 *	0.3	-0.2 *
S14	0.0516380	0.0510466	0.0466089	0.1141255	0.1036708	-0.1 *	-0.5 *	0.0 *	0.1	0.0 *
S15	0.0516445	0.0508458	0	0.1142047	0.1037844	-0.1 *	**-2.5** *	0	0.2	0.1 *
S16	0	0	0	0.1196809	0	0	0	0	0	0
F sum	1.0000000	1.000000	1.0000000	1.0000000	1.0000000					

4.3 Heat Transfer Exchange

For the view factors including the detector at the different locations (Fig 4), the MCRT of multiple zones was used emitting $1x10^6$ rays from each sub-surface and spending up to 200 minutes of CPU time. It was found an almost unchanged value of view factors among the 14 sub-surfaces of Fig. 1 when the detector is relocated (differences less to 10^{-3} falling within the simulation error) because of the small detector area. Thus, for the heat transfer simulations the view factors among the 14 sub-surfaces in all the detector locations remain equal, only the view factors directly related with the detectors sub-surfaces were changed at each location, i.e.: the view factors re-simulated emitting rays from one of the surfaces of the detector (for instance F(16,j)), the view factors of the counter-face (F(8,j)) computed by symmetry relations and lastly the view factors emitting rays from other sub-surfaces to the detector surfaces (F(i,8) and F(i,16)) computed by reciprocity relations. Notice that, in the case of the sub-surfaces with view factors changed by reciprocity relations, the sum rule equal to 1,000000 (see Table 2) will be changed as well, but because of the lower values of the view factors replaced, it changes in less than $1x10^{-3}$,which can be neglected.

Initially, the non-dimensional net fluxes absorbed by each cavity sub-surface and by the detector in relation to the flux emitted by the burner sub-surface ($REF_{n,i}$) were evaluated at three locations of the detector (G, C and RBo). As expected the fluxes that only show sensitivity to the detector location were that received by the detector itself

($REF_{n,8}$ and $REF_{n,16}$) because of its small area. Figure 7 illustrate preliminary results with all the sub-surfaces at three locations (C, G and RBo) showing this sensitivity. The non-dimensional net fluxes absorbed by each cavity sub-surface and by the detector in relation to the flux emitted by the burner sub-surface ($REF_{n,i}$) are illustrated in Fig. 7.a. The largest flux was absorbed by the detector oriented to the burner (sub-surface 8) at the center location (70% of the burner emission) while in the corner of cavity it was 30%. On the other hand, the heat reflected with the superior half of cavity and absorbed by the hypothetic detector oriented to the top of cavity (sub-surface16) results in similar values for the three locations (23±1%) and also it still higher than the largest fluxes absorbed by the cavity sub-surfaces. Lastly, in relation to the net fluxes absorbed by the cavity sub-surfaces, it is worth to highlight: Firstly, the significantly loss of heat with the oven door (glass side) in relation to the back wall, mainly evidenced on simulation with the sub-surface 7 absorbing a flux superior to 30%; and secondly, the asymmetry of fluxes given between the left and right of the bottom of cavity (9% and 4% for sub-surfaces 2 and 3 respectively) which it was not repeated on the superior half of cavity as it can be seen with almost the same values for sub-surfaces 10 to 13. Notice that these thermal asymmetries are in concordance with the non-dimensional temperatures shown in Fig. 2 showing the strong dependence with the fourth power radiation law. Figure 7.b shows the $REF_{i\rightarrow 16}$ for the detector turned to the top of the oven cavity. As it can be seen, the sensitivity of the radiative flux is mainly evidenced comparing the central locations C and G with the RBo location. As it could be anticipated, when the detector is located in the center, the largest flux is received from the burner surface (in G, a second portion come from the glass side with the sub-surface 15), while in the corner the RHT coming from closer sub surfaces (10, 12 and 14) become more important. Also, the total non-dimensional fluxes are approximately 2% superior on center locations that in the corner (24% and 22% for C and RBo respectively).

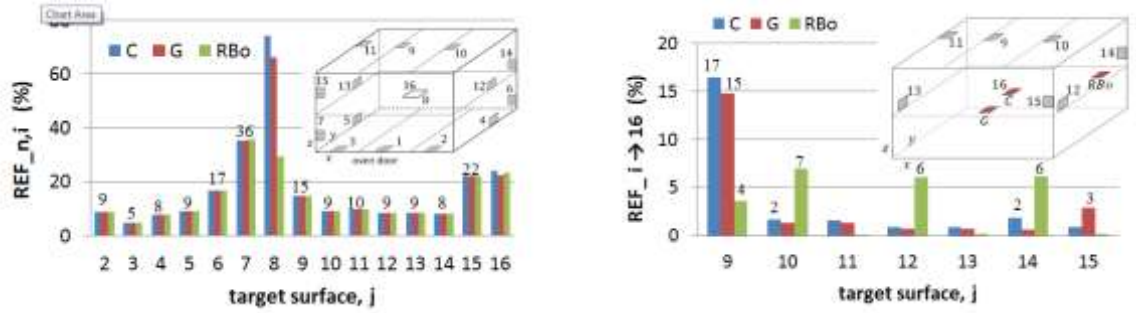

a) b)

Figure 7. Influence of the location of the detector along the plane of the cooking tray (at C, G and RBo) on the REF (a) net absorbed (REF_n,i) by each sub-surface of the oven cavity and detector (sub-surfaces 8 and 16) and (b) absorbed by the detector from the sub-surfaces of the top of the oven cavity (REF i→16).

Once sensitivity of RHT reaching the detector at these locations was verified, the simulations process were extended along the whole plane of the cooking tray, achieving a discrete field of radiation within the oven cavity as it will be briefly illustrated as follows. Firstly are distinguished the partial RHT coming from certain sub-surfaces to subsequently show the total REF from each half of cavity reaching the detector at both orientations, to the top and to the burner sides of cavity. Notice that in the first case with only one sub-surface as source of radiation, and subsequently one mean temperature and emittance, the flux will depend only of the view factor distribution. Thus, the sensitivity of the flux coming from each sub-surface to the view factors at each location can be also observed on this part. Figure 8a shows the REF for the radiative heat exchange between the superior back wall of the cavity and the detector at the different locations. Likewise, the partial RHT in the inferior half of cavity from the sub-surface 3 to the detector is illustrated in 8.b. The flux reaching the detector is plotted on an area of 40x40 mm^2 (absolute oven scale) at each location and the areas of the cooking tray and cavity are delimited with brown and blue respectively. As defined in Eq.(7) the values plotted on the figures represents the percentage of flux reaching each location in relation to the total source of radiative power in the oven, for this case the radiative flux emitted from the burner sub-surface. As it can be seen, the highest fluxes absorbed by the detector are in the closer locations of the source sub-surface, around 6% and 5% in Fig. 8.a and Fig. 8.b respectively. This tendency is repeated along all the partial fields of radiation from each one of the sub-surfaces of the oven studied because of the directly dependence with the view factors.

Fig. 9 shows the maximum values reached from each one of the cavity sub-surfaces at each orientation of the detector in order to have a global illustration of the thermal behavior of the oven tested experimentally. A thermal asymmetry is evidenced between the back and glass sides of the cavity mainly denoted in the inferior half of cavity with around 4.4% (difference of highest REF between S6 and S7). This relation is repeated with the RHT reflected from the superior half of cavity to the detector turned to the top, with a difference around of 3.1%. Between the right and left sides of the bottom cavity (S2 and S3) also an asymmetry occurs with a difference around of 1.5%. Lastly, it is worth to remark the high fluxes absorbed from the superior half of cavity (irrespective the burner sub-surface flux) than from the inferior, as it can be also seen later on with the total REF. The strong difference between inferior and superior sides of cavity is attributed to the gradients of temperature with each sub-surface and the level of uniformity of the radiative flux

reached at both orientations of the detector (see Fig. 2 and Fig. 9). A measure of this uniformity could be seen in the following results with the total fields of radiation within the cavity.

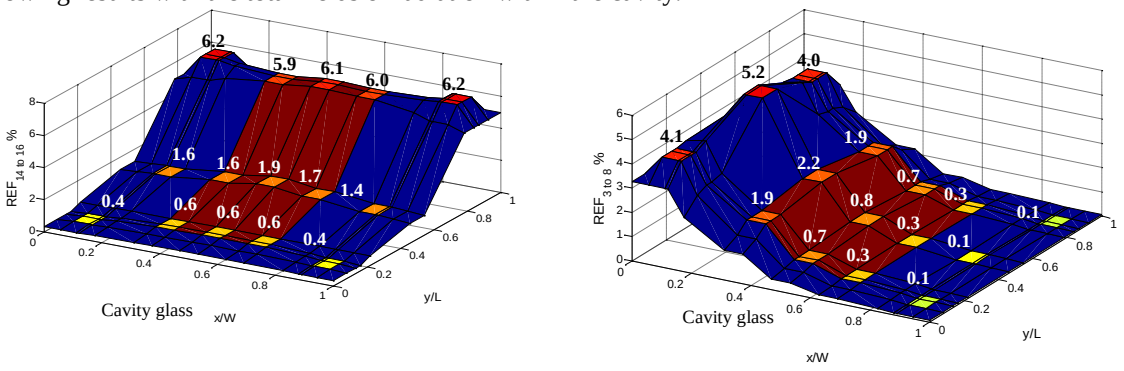

a) b)

Figure 8 Partial fields of radiation a) from the back wall (sub-surface 14) to the detector turned to the top of the oven cavity and b) from the left wall (sub-surface 3) to the detector turned to the burner of the oven cavity

			S6	5.6							
S5	4.7	S3	5.2	S1	70.3	S2	3.7	S4	4.8		
			S7	1.2							

(a)

			S6	6.2							
S5	6.2	S3	9.2	S1	16.7	S2	9.3	S4	6.1		
			S7	3.1							

(b)

Figure 9. Schematic of the maximum REF reached on the whole cavity

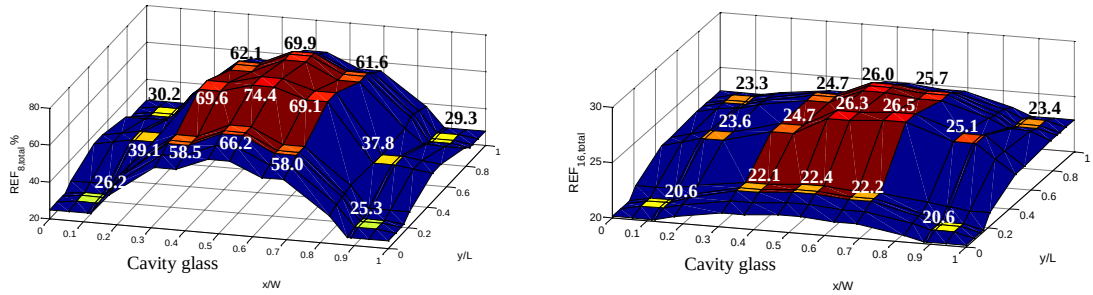

a) b)

Figure 10. Total field of radiation to the detector at both orientations: a) turned to the burner of the oven cavity b) turned to the top of the oven cavity

In Fig. 10.a, the total REF field adding those REF fields reached from sub-surfaces 1 to 7 is illustrated, likewise the 10.b shows the total REF field from sub-surfaces 9 to 15. Comparing a) and b) it can be seen the different ranges of variation in each field, from 25% to 75% for the detector turned to the burner and from 20 to 27% when it is turned to the top of cavity. As it can be anticipated, these total fields of radiation can be seen as the REF for each face of a hypothetic load on the cooking tray plane within the oven. As a measure of the uniformity along a considered face of the load Shaughnessy and Newborough (1998) proposed a coefficient of variation (COV) calculated by the standard deviation relative to the mean of the exchange factors along this face. On this work, in the whole field of total REF the mean values with the detector to the burner and to the top (or for the upper and lower faces of load) were 51.8% and 23.8% respectively, and the COV's were 35% and 8% as well. On the other hand, for only the cooking tray area (color brown in figures) the COV's at both orientations were very closer to each other, 9% and 7% for lower and upper faces respectively, while between the mean REF's still a strong gradient of the whole field: 65.5% on the upper face and 24.5% on the lower face of load.

The present results are comparable to those given by Shaughnessy and Newborough (1998) for electrical ovens in a configuration from one up to four heating elements located in front of different walls within the cavity, specifically when the tray is at a distance (z_p) of 0.16 m to the heating element (our distance to burner sub-surface). The non-dimensional area of the cooking tray in relation to surface source areas (regarding heating element wall area in that work and sub-surface 1 here) is equal to 0.56 in both works. Thus, the mean total REF with the lower side of the load was around 15% higher in the burner oven than in the oven with one heating element (65% of our simulation against 50% with heating elements of different shapes). It can be interpreted as a higher usage of the flux emitted by the power source of the oven when it has a burner instead of heating elements. Moreover, the COV's reached here (9%) were also higher than those reached with all the heating element shapes modeled (all less to 5%). Thus, the electric oven showed more uniformity of the radiation field upon the lower face of the cooking tray than that reached with the gas oven. Lastly, comparing the exchange factors of both faces reached with those achieved in the electric oven with other configurations (heating elements bin front of two and four walls of the cavity), in the upper face with two heating

elements (top and bottom walls) the exchange factor was higher in around 8% than in our simulations (33% against 24.5%), on the other hand in the lower face with four heating elements (top, bottom and lateral walls) the exchange factor was lower around 37% (65% against 28%) than in the burner case. It evidenced the higher differences between the fields of radiation at both sides of cavity (upon and under the cooking tray) found on the burner oven when it is compared with the heating elements oven.

6. CONCLUDING REMARKS

This work developed a Monte Carlo simulation of the thermal radiation exchange among surfaces of a rectangular cavity blocked by a cooking tray, in order to calculate view factors and net radiation heat transfer rates and to evaluate proportions and uniformity of radiation reaching a load on the interior of a domestic gas oven. The boundary conditions for radiative simulations were provided by measurements in a typical commercial gas oven. The surface and time averaged temperatures used in simulations keep the thermal behavior trends within the oven, for instance higher driving forces with glass wall and bottom plate. For the view factor simulations, a ray tracing algorithm is implemented and validated for different configurations showing the feasibility of the method proposed. A convergence analysis of simulations is done with available solutions achieving high accurate results even for 10^4 rays emitted and reaching almost the same spread gradients over the number of rays for all the test configurations. The spread results also evidenced a proportionate dependence with the magnitude of the mean view factors. As it can be expected, higher view factors imply higher spatial uncertainty and higher spread as well. In the algorithm implemented by the multi-zones approach, rays were traced among multiple surfaces in geometries with obstacles allowing the computing of multiple view factors simultaneously. The simplified input definition of surfaces coordinates resulted in a substantially reduction of time required for simulations. Accurate results were also reached. The field of radiation on the interior of cavity for the net heat transfer rates from 14 sub-surfaces of cavity confirms the strong dependence with the fourth power radiation law showing thermal asymmetries in concordance with the field of temperatures. In the partial RHT from each sub-surface to cooking tray regions, the sensitivity to view factors distribution is clearly evidenced and the stronger difference at both orientations of detector is attributed to the different gradients of temperature. In the total REF the quantitative comparison with an electric oven indicates that a higher proportion of radiation reaches the load surfaces in the burner gas oven but with lower uniformity than that reached with heating elements. Finally, it is worth to remark that regarding the results for the currently tested gas oven the method proposed can be applied as well to other geometries of cavity, cooking tray locations and finishing of surfaces in order to find the preferred configurations with higher values of REF and lower COV seek in ovens design.

5. REFERENCES

Cheng, Z. D., He, Y. L., & Cui, F. Q., 2013. “A new modelling method and unified code with MCRT for concentrating solar collectors and its applications”. Applied Energy, Vol. 101, pp. 686–698.

Coelho, P. J., Goncalves, J. M., & Carvalho, M. G., 1998. “Modelling of radiative heat transfer in enclosures with obstacles”. International Journal of Heat and Mass Transfer, Vol. 41, pp. 745–756.

Howell, J. R., 2010. A catalog of radiation heat transfer configurations factors. Retrieved June 01, 2015, from http://www.thermalradiation.net

Luo, X., Hauer, V., & Day, C., 2012. “Monte Carlo calculation of the thermal radiation heat load of the ITER pre-production cryopump”. Fusion Engineering and Design, Vol. 87, No. 5-6, pp. 603–607.

Maurente, A. , 2007. Método de Monte Carlo aplicado ao modelamento espectral de meios participantes através da utilização da função de distribuição de energia de corpo negro nas linhas de absorção. PhD Thesis. Universidade Federal de Rio Grande do Sul. Porto Alegre, RS, Brazil.

Modest, M. F., 2003. Radiative heat transfer. A. Press, Ed. 2nd ed., p. 822. Academic Press.

Nellis, G., & Klein, S., 2009. Heat transfer. C. U. Press, Ed. pp. 979–1088. Cambridge University Press.

Oliveira, A. A. M., 2014. Radiation view factors for radiation exchange within an oven cavity with and without obstacles (in portuguese). , Report, Labcet - UFSC.

Oliveira, A. A. M., & Pereira, F. M., 2011. Heat transfer in oven cavities. Report, LABCET- UFSC.

Shaughnessy, B. M., & Newborough, M., 1998. “Radiative heat transfer in low-emissivity ovens”. Applied Thermal Engineering, Vol. 18, No. 8, pp. 619–641.

Siegel, R., & Howell, J. R., 1992. Thermal radiation heat transfer. 3rd ed., p. 1072. Taylor and Francis.

Torres, J. A., 2015. Monte Carlo simulation of radiative heat transfer in cavities of domestic gas ovens. M.Sc. Dissertation, Federal University of Santa Catarina, Florianópolis, SC, Brazil.

Viskanta, R., & Toor, J. S., 1968. “A numerical experiment of radiant heat interchange by the monte carlo method”. International Journal of Heat and Mass Transfer, Vol. II, pp. 883–897.

Wang, A., & Modest, M. F., 2007. “Spectral Monte Carlo models for nongray radiation analyses in inhomogeneous participating media”. International Journal of Heat and Mass Transfer, Vol. 50, No. 19-20, pp. 3877–3889.